Electromagnetic dispersion modeling and measurements for HVDC power cables

Nordebo, Sven; Nilsson, Börje; Biro, Thomas; Cinar, Gökhan; Gustafsson, Mats; Gustafsson, Stefan; Karlsson, Anders; Sjöberg, Mats

2011

CODEN:LUTEDX/(TEAT-7211)/1-32/(2011)

Electromagnetic dispersion modeling and measurements for HVDC power cables

Sven Nordebo, Börje Nilsson, Thomas Biro, Gökhan Cinar, Mats Gustafsson, Stefan Gustafsson, Anders Karlsson, and Mats Sjöberg

Electromagnetic Theory
Department of Electrical and Information Technology
Lund University
Sweden

Sven Nordebo, Börje Nilsson, Stefan Gustafsson
{sven.nordebo,borje.nilsson,stefan.h.gustafsson}@lnu.se

School of Computer Science, Physics and Mathematics
Linnaeus University
SE-351 95 Växjö
Sweden

Thomas Biro
thomas.biro@jth.hj.se

School of Engineering
Jönköping University
SE-551 11 Jönköping
Sweden

Gökhan Cinar
gokhan_cinar@yahoo.com

Electronics Engineering Department
Gebze Institute of Technology
414 00 Gebze, Kocaeli
Turkey

Mats Gustafsson, Anders Karlsson
{mats.gustafsson,anders.karlsson}@eit.lth.se

Department of Electrical and Information Technology
Electromagnetic Theory
Lund University
P.O. Box 118
SE-221 00 Lund
Sweden

Mats Sjöberg
mats.l.sjoberg@se.abb.com

ABB AB
SE-371 23 Karlskrona
Sweden

Editor: Gerhard Kristensson

Abstract

This paper provides a general framework for electromagnetic modeling, computation and measurements regarding the wave propagation characteristics of High-Voltage Direct Current (HVDC) power cables. The modeling is focused on very long (10 km or more) HVDC power cables and the relevant frequency range is therefore in the low-frequency regime of about 0-100 kHz. An exact dispersion relation is formulated together with a discussion on practical aspects regarding the computation of the propagation constant and the related characteristic impedance. Experimental time-domain measurement data from an 80 km long HVDC power cable is used to validate the model. It is concluded that a single-mode transmission line model is not adequate to account for the mismatch between the power cable and the instrumentation. A mismatch calibration procedure is therefore devised to account for the connection between the measurement equipment and the cable. A dispersion model is thus obtained that is accurate for early times of pulse arrival. To highlight the potential of accurate electromagnetic modeling, an example of high-resolution length-estimation is discussed and analyzed using statistical methods based on the Cramér-Rao lower bound. The analysis reveals that the estimation accuracy based on the present model (and its related model error) is in the order of 100 m for an 80 km long power cable, and that the potential accuracy using a "perfect" model based on the given measurement data is in the order of centimeters.

1 Introduction

Power cables are usually designed for the single purpose of carrying power at 0 Hz, 50 Hz or 60 Hz, with little or no regard to losses at higher frequencies. However, there are numerous existing and potential high-frequency applications for signal transmission on power cables, as *e.g.*, with power line communication (PLC) techniques [28], simulation and analysis of lightning and switching overvoltages [28], transient based protection [2] and fault localization and Partial Discharge (PD) monitoring [24, 29, 32]. The present study is motivated in particular by the potential of improving the fault localization and diagnosis techniques for High-Voltage Direct Current (HVDC) submarine power cables based on detection and analysis of transient (virgin) pulses caused by dielectric breakdown. A systematic study and accurate modeling of the fundamental dispersion and attenuation behavior of lossy coaxial cables is of great importance in these applications.

The theory and applications for traveling waves on transmission lines and power cables is a classical and well established research area, see *e.g.*, [5, 8, 16, 17, 22, 30]. In particular, it has been of great interest recently to study measurements and modeling regarding the semiconducting layers of a power cable and its effect on wave propagation characteristics [1, 3, 28]. It has been shown, *e.g.*, that the semiconducting layer contributes significantly to the attenuation for frequencies above 5-10 MHz [28].

Many of the classical results such as in [1, 5] are based on approximations and restrictions rather than on accurate numerical solutions of the electromagnetic problem

and the related dispersion relation. Hence, in [1, 5], low-frequency approximations are incorporated where the longitudinal wave number is partly neglected and the exact dispersion relation is avoided. These approximations may not be sufficiently accurate if a precise evaluation is required with respect to the dispersion properties of a multi-layered coaxial power cable.

It can be shown that the low-frequency asymptotics of the propagation constant of a coaxial cable with one insulating layer is given by $\gamma \sim A\sqrt{\mathrm{i}\omega/\mathrm{c}_0}$ when the frequency $\omega \to 0$ and where A is a real and positive constant [19]. It is also concluded in [19] that if an accurate low-frequency solution is required in a particular HVDC power cable application, the first order asymptotic expansion is not accurate enough over a relevant bandwidth, and a numerical solution to the dispersion relation is hence very useful.

The purpose of this paper is to provide a general framework for electromagnetic modeling, computation and measurements regarding the wave propagation characteristics of HVDC power cables. The computational framework is employed here in connection with time-domain measurements, but can easily be adapted to frequency domain measurements such as with Frequency Modulated Continuous Wave (FMCW) modules, Vector Network Analyzers (VNA), etc. The modeling is focused on very long (10 km or more) HVDC power cables and the relevant frequency range is therefore in the low-frequency regime of about 0-100 kHz. The electromagnetic model is validated by using experimental time-domain measurement data from an 80 km long HVDC power cable. It is found that a single-mode transmission line model is not adequate to obtain a good fit between the measurements and the model, and a mismatch calibration procedure is therefore devised to account for the connection between the measurement equipment and the power cable. An example of high-resolution length-estimation is finally analyzed to highlight the potential of accurate electromagnetic modeling.

The rest of the paper is organized as follows: Section 2 describes the measurement set-up, the basic transmission line modeling and the mismatch calibration procedure. Section 3 gives the electromagnetic model and the exact dispersion relation together with a discussion on practical aspects regarding the computation of the propagation constant and the related characteristic impedance. Section 4 contains the experimental and numerical examples and section 5 the summary and future work. Appendix A describes the time-domain modeling by using the FFT (Fast Fourier Transform) and frequency weighting to avoid the Gibbs phenomena in the time-domain. Finally, Appendix B defines the cylindrical vector waves.

2 Measurements and modeling

2.1 Measurement set-up and basic transmission line modeling

Consider the time-domain measurement set-up as illustrated in Figure 1. The basic measurement equipment is a standard sampling oscilloscope and a pulse generator.

The pulse generator voltage is denoted V_s and the measured voltage at the oscilloscope V. The characteristic impedance of the HVDC power cable is denoted Z and the propagation constant γ, see *e.g.*, [10, 25]. The length d of the power cable is typically in the order of hundreds of kilometers. The cable is terminated with an impedance Z_L. During the measurements, the pulse generator and the oscilloscope were connected to the power cable using a standard coaxial cable with impedance $R_0 = 50\,\Omega$ and length $d_0 \approx 10\,\mathrm{m}$. Two specially designed shielded connections were used to connect to either end of the extruded HVDC power cable for a minimum of disturbances and noise, see Figure 2. The internal resistance of the pulse generator was shunted to $R = 25\,\Omega$ for better matching. During the measurements, the far-end of the power cable was either left open with $Z_\mathrm{L} = \infty$, or matched with $Z_\mathrm{L} = R$.

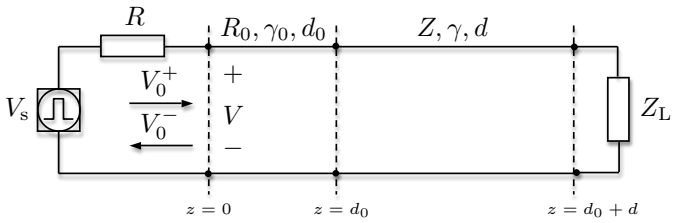

Figure 1: Measurement set-up and transmission line model. The pulse generator voltage is denoted V_s and the measured voltage V at the oscilloscope consists of a transmitted and a reflected wave amplitude $V = V_0^+ + V_0^-$.

Figure 2: Shielded connection to the extruded HVDC power cable. The armour of the power cable has been opened and the standard coaxial cable is connected to the inner conductor and the lead sheat of the power cable.

Let the time- and space-convention for a propagating wave in the z-direction of the cable be given by $\mathrm{e}^{\mathrm{i}\omega t}\mathrm{e}^{-\gamma z}$ where t is the time, $\omega = 2\pi f$ the angular frequency, f the frequency and γ the propagation constant. Assuming that the effect of the standard coaxial cable can be neglected ($d_0 \ll d$), the reflection coefficient as seen by the forward traveling wave at the generator intersection at $z = 0$, is given by

$$\Gamma = S_{11} + \frac{S_{21}S_{12}\Gamma_\mathrm{L}\mathrm{e}^{-2\gamma d}}{1 + S_{11}\Gamma_\mathrm{L}\mathrm{e}^{-2\gamma d}}, \tag{2.1}$$

where the basic reflection and transmission parameters of the connection are $S_{11} = (Z-R)/(Z+R)$, $S_{12} = 2R/(Z+R)$ and $S_{21} = 2Z/(Z+R)$ and $\Gamma_{\rm L} = (Z_{\rm L}-Z)/(Z_{\rm L}+Z)$ is the reflection coefficient at the load, *cf.*, [25]. The observed voltage V at the oscilloscope can hence be expressed as

$$V = V_0^+ + V_0^- = V_0^+(1+\Gamma) \tag{2.2}$$

where V_0^+ and V_0^- are the wave amplitudes of the forward and backward traveling waves defined at the generator side, respectively.

From a geometric series expansion in (2.1), the voltage V in (2.2) can also be expressed as

$$V = V_0^+ \left(1 + S_{11} + S_{21}S_{12}\Gamma_{\rm L}{\rm e}^{-2\gamma d} + \cdots\right) \tag{2.3}$$

in a series of multiply reflected and transmitted pulses[1]. In the reflection measurement described below, the far-end of the cable was left open and it is hence assumed that $\Gamma_{\rm L} = 1$. By neglecting the effect of the coaxial cable (let $d_0 = 0$), and only considering the first two consecutively observed pulses $V^{(1)}$ and $V^{(2)}$ in (2.3), the following model is obtained for the observed voltage at the oscilloscope

$$V = V^{(1)} + V^{(2)} \tag{2.4}$$

where

$$\left\{ \begin{array}{rcl} V^{(1)} & = & V_0^+(1+S_{11}) \\ V^{(2)} & = & V_0^+ S_{21}S_{12}{\rm e}^{-2\gamma d} \end{array} \right. \tag{2.5}$$

and where the parameters S_{11}, S_{21}, S_{12} and γ have been defined above.

Note that V_0^+ and V_0^- represent a wave splitting with respect to the internal resistance R at the generator side where $V = V_0^+ + V_0^-$, $RI = V_0^+ - V_0^-$ and $V = V_{\rm s} - RI$ where I is the current. Hence

$$V_0^+ = V_{\rm s}/2 \tag{2.6}$$

is the amplitude of the forward traveling wave which is incident at the intersection at $z = 0$. In the present experimental set-up, the generator was set to generate a rectangular pulse with amplitude $V_{\rm s0}$ and pulse-width $T_{\rm p}$. The pulse repetition time was very long and can hence be neglected. The Fourier spectrum of the pulse is then given by

$$V_{\rm s} = V_{\rm s0}T_{\rm p}{\rm e}^{-{\rm i}\omega T_{\rm p}/2}\frac{\sin(\omega T_{\rm p}/2)}{\omega T_{\rm p}/2}. \tag{2.7}$$

Provided that the characteristic parameters γ and Z of the power cable are given, the frequency domain model (2.4)–(2.5) based on single-mode transmission line theory is now complete. An Inverse Fast Fourier Transformation (IFFT) [21, 27] is used to obtain the time-domain voltage amplitude $v(t)$ corresponding to the modeled frequency domain response (2.4). The most important definitions and properties regarding the IFFT and the rejection of the Gibbs phenomena in the time-domain are summarized in the Appendix A.

[1]Note that the terminology "pulses" is employed here for convenience, even though the representation refers to the frequency domain.

2.2 Mismatch calibration

The mismatch modeling described above is valid only if the wave propagation phenomena on the two cables can be represented by single modes with impedances Z and R, respectively. In practice, however, there will exist a multiple-mode excitation at the connection between the measurement cable and the power cable. There are several mode-matching techniques that could potentially be used to model the corresponding mismatch, see *e.g.*, [7]. Here, a simple mismatch calibration procedure is proposed as follows:

Let S_{11} and S_{21} and S_{12} denote the scattering parameters of the cable connection (as seen from the measurement instrumentation) and which are related to the dominating modes of the two connecting waveguides. It is assumed that the connections at both ends of the power cable are identical. Two measurements are conducted based on reflection and transmission, respectively. In the reflection measurement, a wave amplitude $V_{0\mathrm{r}}^{+}$ is transmitted at the near-end of the power cable with the far-end left open, and it is hence assumed that $\Gamma_{\mathrm{L}} = 1$. The signal measured at the near-end is time-gated to remove the first reflection $V_{0\mathrm{r}}^{+}(1 + S_{11})$, and the resulting reflection measurement can hence be modeled as

$$V_{\mathrm{r}} = V_{0\mathrm{r}}^{+} S_{21} S_{12} \mathrm{e}^{-2\gamma d}. \tag{2.8}$$

If time-domain measurements are available, the time-gating can be performed directly on the observed data. If frequency domain measurements are available such as with the VNA, an inverse Fourier transformation needs to be executed first.

In the transmission measurement, a wave amplitude $V_{0\mathrm{t}}^{+}$ is transmitted at the near-end of the power cable with the far-end matched with $Z_{\mathrm{L}} = R$. Since the two connections are assumed to be identical, the signal measured at the far-end can be modeled as

$$V_{\mathrm{t}} = V_{0\mathrm{t}}^{+} S_{21} S_{12} \mathrm{e}^{-\gamma d}. \tag{2.9}$$

The two measurements (2.8) and (2.9) represent a nonlinear system of equations with the unique solution

$$\begin{cases} \widehat{S_{21}S_{12}} &= \dfrac{V_{\mathrm{t}}^{2} V_{0\mathrm{r}}^{+}}{V_{\mathrm{r}} V_{0\mathrm{t}}^{+2}} \\ \widehat{\mathrm{e}^{-\gamma d}} &= \dfrac{V_{\mathrm{r}} V_{0\mathrm{t}}^{+}}{V_{\mathrm{t}} V_{0\mathrm{r}}^{+}} \end{cases} \tag{2.10}$$

provided that the denominators in (2.10) are nonzero.

Assuming that the calibration measurement outlined above can be performed with high accuracy, the dispersion model based on mismatch calibration is finally given by

$$V_{\mathrm{t}} = V_{0\mathrm{t}}^{+} \widehat{S_{21}S_{12}} \mathrm{e}^{-\gamma d} \tag{2.11}$$

where the propagation constant γ is given by an electromagnetic model.

3 Electromagnetic modeling and computation

3.1 The propagation constant and dispersion relation

Let μ_0, ε_0, η_0 and c_0 denote the permeability, the permittivity, the wave impedance and the speed of light in free space, respectively, and where $\eta_0 = \sqrt{\mu_0/\varepsilon_0}$ and $\mathrm{c}_0 = 1/\sqrt{\mu_0\varepsilon_0}$. The wave number of free space is given by $k = \omega/\mathrm{c}_0$ where $\omega = 2\pi f$ is the angular frequency and f the frequency. It follows that $\omega\mu_0 = k\eta_0$ and $\omega\varepsilon_0 = k/\eta_0$. The cylindrical coordinates are denoted by (ρ, ϕ, z), the corresponding unit vectors $(\hat{\boldsymbol{\rho}}, \hat{\boldsymbol{\phi}}, \hat{\boldsymbol{z}})$ and the transversal coordinate vector $\boldsymbol{\rho} = \rho\hat{\boldsymbol{\rho}}$. The time-convention is defined by the factor $\mathrm{e}^{\mathrm{i}\omega t}$.

Let $\boldsymbol{E}$ and $\boldsymbol{H}$ denote the electric and magnetic fields, respectively. The source-free Maxwell's equations [10] are given in the frequency domain as

$$\begin{cases} \nabla \times \boldsymbol{E} = -\mathrm{i}\omega\mu_0\boldsymbol{H} \\ \nabla \times \boldsymbol{H} = \mathrm{i}\omega\varepsilon_0\epsilon\boldsymbol{E}, \end{cases} \tag{3.1}$$

where ϵ is the complex permittivity of the material given by

$$\epsilon = \epsilon_\mathrm{r} - \mathrm{i}\frac{\sigma}{k}\eta_0, \tag{3.2}$$

and where ϵ_r is the real, relative permittivity and σ the conductivity.

The present study is concerned with the eigenvalue (or modal) solutions to Maxwell's equations (3.1) for a multi-layered circularly symmetrical cylindrical waveguide. The wave propagation along the z-direction of the waveguide is given by the exponential factor $\mathrm{e}^{-\gamma z}$ where γ is the propagation constant corresponding to a particular mode [10, 25]. With $\boldsymbol{E} = \boldsymbol{E}(\boldsymbol{\rho}, \gamma)\mathrm{e}^{-\gamma z}$ and $\boldsymbol{H} = \boldsymbol{H}(\boldsymbol{\rho}, \gamma)\mathrm{e}^{-\gamma z}$, the eigenvalue problem to be solved is given by

$$\left\{\nabla_\mathrm{t}^2 + k^2\epsilon + \gamma^2\right\} \begin{Bmatrix} \boldsymbol{E}(\boldsymbol{\rho}, \gamma) \\ \boldsymbol{H}(\boldsymbol{\rho}, \gamma) \end{Bmatrix} = \begin{Bmatrix} \mathbf{0} \\ \mathbf{0} \end{Bmatrix} \tag{3.3}$$

together with the appropriate boundary conditions, and where ∇_t^2 is the transversal part of the Laplace operator and γ^2 the eigenvalue [10, 25].

A practical approach to derive the appropriate boundary conditions is to employ the cylindrical vector wave expansion as defined in Appendix B. Hence, to find the eigenvalues, it is noted that the partial wave expressions under the integrals in (B.5) and (B.6) satisfy (3.3), and it only remains to find non-trivial solutions satisfying the appropriate boundary conditions. It should be noted, however, that the eigenvalue problem (3.3) in general has a continuous spectrum if an exterior infinite domain is included. This complication is also manifested by the presence of branch-cuts in the complex γ-plane related to the path integrals (B.5) and (B.6) defined in Appendix B.

The present study is concerned with the Transversal Magnetic (TM) modes of order $m = 0$ denoted TM_{0n}, as the Transversal Electric (TE) modes of order $m = 0$, TE_{0n}, and all the higher order modes with $m \neq 0$ will essentially be cut-off in the low-frequency regime. In particular, the first TM_{01} mode of main interest is also called

the quasi-TEM mode as it constitutes an approximation of the TEM mode of a single layered coaxial cable with permittivity $\epsilon_{\rm d}$ and propagation constant $\gamma = {\rm i}k\sqrt{\epsilon_{\rm d}}$, see also [25]. It should be noted that for a multi-layered circular waveguide, the Transversal Electric (TE) and Transversal Magnetic (TM) field components are generally coupled via the boundary conditions, but are always decoupled for the axial symmetric TM_{0n} and TE_{0n} modes.

Consider a multi-layered circularly symmetrical cylindrical waveguide as depicted in Figure 3. There are $N+1$ material boundaries with radius ρ_i for $i = 0, 1, \ldots, N$ defining an inner region for $0 \leq \rho \leq \rho_0$ with permittivity ϵ_0, N intermediate layers for $\rho_{i-1} \leq \rho \leq \rho_i$ with permittivity ϵ_i for $i = 1, \ldots, N$ and an outer region for $\rho \geq \rho_N$ with permittivity ϵ_{N+1}.

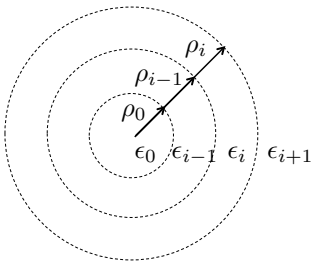

Figure 3: The multi-layered circularly symmetrical cylindrical waveguide (coaxial cable) with geometrical and material definitions.

The complex valued permittivity in each of the $N+2$ regions are defined by

$$\epsilon_i = \epsilon_{{\rm r}i} - {\rm i}\sigma_i\eta_0/k, \;\; i = 0, 1, \ldots, N+1, \tag{3.4}$$

where $\epsilon_{{\rm r}i}$ is the corresponding real, relative permittivity and σ_i the conductivity. Let

$$\kappa_i = \sqrt{k^2\epsilon_i + \gamma^2}, \;\; i = 0, 1, \ldots, N+1, \tag{3.5}$$

be the corresponding radial wave number for material region i where the square root[2] is chosen such that $\mathrm{Im}\,\kappa_i \leq 0$, see also Appendix B.

The electric and magnetic field components are given by the expansion in cylindrical vector waves (B.2), (B.5) and (B.6) defined in Appendix B. For the TM_{0n} modes, the non-zero field components are given in each layer by

$$E_z = \frac{1}{2\pi{\rm i}}\frac{\kappa}{k}\left[a\psi_0^{(1)}(\kappa\rho) + b\psi_0^{(2)}(\kappa\rho)\right]{\rm e}^{-\gamma z} \tag{3.6}$$

$$E_\rho = \frac{1}{2\pi{\rm i}}\frac{\gamma}{k}\left[a\psi_1^{(1)}(\kappa\rho) + b\psi_1^{(2)}(\kappa\rho)\right]{\rm e}^{-\gamma z} \tag{3.7}$$

$$H_\phi = \frac{1}{2\pi\eta_0}\epsilon\left[a\psi_1^{(1)}(\kappa\rho) + b\psi_1^{(2)}(\kappa\rho)\right]{\rm e}^{-\gamma z} \tag{3.8}$$

[2]If the square root has positive real part, *i.e.*, $\mathrm{Re}\,\sqrt{\cdot} \geq 0$ such as with the MATLAB software, then κ is chosen as $\kappa = -{\rm i}\sqrt{-k^2\epsilon - \gamma^2}$ to guarantee that $\mathrm{Im}\,\kappa \leq 0$.

where a and b are complex valued expansion coefficients and $\psi_m^{(j)}(\cdot)$ a Bessel function or a Hankel function of the first kind ($j = 1$) and the second kind ($j = 2$) and order m. Here, the relation $\psi_0^{(j)\prime}(\cdot) = -\psi_1^{(j)}(\cdot)$ [20] has also been used.

For the intersection between two materials with finite conductivity[3] the appropriate boundary conditions are given by the continuity of the tangential electric and magnetic fields [10]. For the TM_{0n} modes these boundary conditions can now be formulated using (3.6) and (3.8) as follows. Let a_0, a_i and b_i for $i = 1, \ldots, N$ and b_{N+1} denote the expansion coefficients corresponding to the $N + 2$ regions defined above. The boundary conditions related to the inner boundary at radius ρ_0 are given by

$$\begin{cases} a_1\kappa_1 \mathrm{H}_0^{(1)}(\kappa_1\rho_0) + b_1\kappa_1 \mathrm{H}_0^{(2)}(\kappa_1\rho_0) - a_0\kappa_0 \mathrm{J}_0(\kappa_0\rho_0) = 0 \\ a_1\epsilon_1 \mathrm{H}_1^{(1)}(\kappa_1\rho_0) + b_1\epsilon_1 \mathrm{H}_1^{(2)}(\kappa_1\rho_0) - a_0\epsilon_0 \mathrm{J}_1(\kappa_0\rho_0) = 0 \end{cases} \tag{3.9}$$

where $\mathrm{J}_m(\cdot)$ denotes the Bessel function of the first kind and $\mathrm{H}_m^{(1)}(\cdot)$ and $\mathrm{H}_m^{(2)}(\cdot)$ the Hankel functions of the first and second kind, respectively, see also the Appendix B. The boundary conditions related to the intermediate boundaries at radius ρ_{i-1} are similarly given by

$$\begin{cases} a_i\kappa_i \mathrm{H}_0^{(1)}(\kappa_i\rho_{i-1}) + b_i\kappa_i \mathrm{H}_0^{(2)}(\kappa_i\rho_{i-1}) \\ -a_{i-1}\kappa_{i-1} \mathrm{H}_0^{(1)}(\kappa_{i-1}\rho_{i-1}) - b_{i-1}\kappa_{i-1} \mathrm{H}_0^{(2)}(\kappa_{i-1}\rho_{i-1}) = 0 \\ a_i\epsilon_i \mathrm{H}_1^{(1)}(\kappa_i\rho_{i-1}) + b_i\epsilon_i \mathrm{H}_1^{(2)}(\kappa_i\rho_{i-1}) \\ -a_{i-1}\epsilon_{i-1} \mathrm{H}_1^{(1)}(\kappa_{i-1}\rho_{i-1}) - b_{i-1}\epsilon_{i-1} \mathrm{H}_1^{(2)}(\kappa_{i-1}\rho_{i-1}) = 0 \end{cases} \tag{3.10}$$

where $i = 2, \ldots, N$. The boundary conditions related to the outer boundary at radius ρ_N are finally given by

$$\begin{cases} b_{N+1}\kappa_{N+1} \mathrm{H}_0^{(2)}(\kappa_{N+1}\rho_N) - a_N\kappa_N \mathrm{H}_0^{(1)}(\kappa_N\rho_N) - b_N\kappa_N \mathrm{H}_0^{(2)}(\kappa_N\rho_N) = 0 \\ b_{N+1}\epsilon_{N+1} \mathrm{H}_1^{(2)}(\kappa_{N+1}\rho_N) - a_N\epsilon_N \mathrm{H}_1^{(1)}(\kappa_N\rho_N) - b_N\epsilon_N \mathrm{H}_1^{(2)}(\kappa_N\rho_N) = 0. \end{cases} \tag{3.11}$$

Note that the inner region is represented solely by the Bessel function $\mathrm{J}_m(\kappa_0\rho)$ (regular wave) in (3.9) and the outer region is represented solely by the Hankel function $\mathrm{H}_m^{(2)}(\kappa_{N+1}\rho)$ of the second kind (outgoing wave) in (3.11), see also Appendix B.

The boundary conditions in (3.9) through (3.11) for all the intersections under consideration are assembled into a square $(2N + 2) \times (2N + 2)$ matrix $\mathbf{A}(\gamma)$, and the corresponding dispersion relation is given by

$$\det \mathbf{A}(\gamma) = 0, \tag{3.12}$$

which is the condition for the existence of a propagating mode [10, 25].

[3]It is assumed that at least one of the layers have non-zero conductivity so that there are no surface currents.

If there exists an initial guess of a particular propagation constant γ_1, the exact value can be computed by the normalized residue

$$\gamma_1 = \frac{\oint_{\mathcal{C}} \frac{\gamma}{\det \mathbf{A}(\gamma)} \, \mathrm{d}\gamma}{\oint_{\mathcal{C}} \frac{1}{\det \mathbf{A}(\gamma)} \, \mathrm{d}\gamma}, \tag{3.13}$$

provided that the closed loop $\mathcal{C}$ is circumscribing the true value γ_1, and that there are no other zeros of $\det \mathbf{A}(\gamma)$ inside the loop. A numerical algorithm to compute the eigenvalue $\gamma_1(k)$ at different wave numbers (frequencies) k can now be formulated by the following basic steps:

1. Determine an initial guess $\hat{\gamma}_1(k_0)$ at the initial wave number k_0.
2. Given the initial guess $\hat{\gamma}_1(k)$ at wave number k, determine a contour $\mathcal{C}$ that is large enough to circumscribe the zero $\gamma_1(k)$ of interest, and small enough to avoid other zeros and branch-cuts.
3. Calculate the zero $\gamma_1(k)$ of interest by using a numerical integration based on (3.13).
4. Given the propagation constant $\gamma_1(k)$ at wave number k, determine an approximate initial guess $\hat{\gamma}_1(k + \Delta k)$ at the next wave number $k + \Delta k$. Return to 2 above, or stop if required.

3.2 The characteristic impedance

To determine the characteristic impedance Z of the power cable, the following quasi-static voltage and current waves are used

$$V^+(z) = \int_{\rho_0}^{\rho_L} E_\rho \, \mathrm{d}\rho \tag{3.14}$$

$$I^+(z) = \int_0^{2\pi} \int_0^{\rho_1} \sigma E_z \rho \, \mathrm{d}\rho \, \mathrm{d}\phi \tag{3.15}$$

where ρ_0 is the radius of the inner conductor, ρ_L the radius of the lead shield and ρ_1 the radius of the inner semi-conducting layer. By using the expression (3.7), the voltage wave can be computed as

$$\begin{aligned} V^+(z) &= \sum_{i=1}^{L} \int_{\rho_{i-1}}^{\rho_i} \frac{-\gamma \mathrm{e}^{-\gamma z}}{2\pi \mathrm{i} k} \left(a_i \mathrm{H}_0^{(1)\prime}(\kappa_i \rho) + b_i \mathrm{H}_0^{(2)\prime}(\kappa_i \rho) \right) \mathrm{d}\rho \\ &= \frac{-\gamma \mathrm{e}^{-\gamma z}}{2\pi \mathrm{i} k} \sum_{i=1}^{L} \left\{ \frac{a_i}{\kappa_i} \left(\mathrm{H}_0^{(1)}(\kappa_i \rho_i) - \mathrm{H}_0^{(1)}(\kappa_i \rho_{i-1}) \right) + \frac{b_i}{\kappa_i} \left(\mathrm{H}_0^{(2)}(\kappa_i \rho_i) - \mathrm{H}_0^{(2)}(\kappa_i \rho_{i-1}) \right) \right\} \end{aligned} \tag{3.16}$$

where the relation $\psi_0^{(j)\prime}(\cdot) = -\psi_1^{(j)}(\cdot)$ has been used ($j = 1, 2$).

By using the expression (3.6), the current wave can be computed as

$$\begin{aligned} I^+(z) &= \frac{\sigma_0}{\mathrm{i}k}\mathrm{e}^{-\gamma z}\int_0^{\rho_0} a_0 \mathrm{J}_0(\kappa_0\rho)\kappa_0\rho\,\mathrm{d}\rho \\ &\qquad + \frac{\sigma_1}{\mathrm{i}k}\mathrm{e}^{-\gamma z}\int_{\rho_0}^{\rho_1}\left(a_1\mathrm{H}_0^{(1)}(\kappa_1\rho) + b_1\mathrm{H}_0^{(2)}(\kappa_1\rho)\right)\kappa_1\rho\,\mathrm{d}\rho \\ &= -\mathrm{i}\sigma_0\frac{a_0}{k}\rho_0\mathrm{J}_1(\kappa_0\rho_0)\mathrm{e}^{-\gamma z} - \mathrm{i}\sigma_1\frac{a_1}{k}\left(\rho_1\mathrm{H}_1^{(1)}(\kappa_1\rho_1) - \rho_0\mathrm{H}_1^{(1)}(\kappa_1\rho_0)\right)\mathrm{e}^{-\gamma z} \\ &\qquad - \mathrm{i}\sigma_1\frac{b_1}{k}\left(\rho_1\mathrm{H}_1^{(2)}(\kappa_1\rho_1) - \rho_0\mathrm{H}_1^{(2)}(\kappa_1\rho_0)\right)\mathrm{e}^{-\gamma z} \end{aligned} \tag{3.17}$$

where the integral $\int \psi_0^{(j)}(x)x\,\mathrm{d}x = x\psi_1^{(j)}(x)$ has been used which is valid for any Bessel or Hankel function $\psi_m^{(j)}(x)$ ($j = 1, 2$), see [20].

Assume that the propagation constant γ_1 of the quasi-TEM TM_{01} mode is given (*i.e.*, has been obtained numerically) for a particular wave number k. The coefficients a_0 and a_i and b_i for $i = 1, \ldots, L$ defining the corresponding voltage and current waves in (3.16) and (3.17) above can then be obtained (as a non-trivial solution) from the nullspace of the matrix $\mathbf{A}(\gamma_1)$ defined in (3.9) through (3.11) above. It is a very sensitive numerical operation to obtain an eigenvector of the matrix $\mathbf{A}(\gamma_1)$ corresponding to its zero eigenvalue, in particular when the wave number k is getting large. A preconditioning of the numerical problem is therefore highly recommended, and one possibility is to proceed as follows:

Let $a_0 = 1$, and move the corresponding terms to the right-hand side of (3.9) yielding

$$\begin{cases} a_1\kappa_1\mathrm{H}_0^{(1)}(\kappa_1\rho_0) + b_1\kappa_1\mathrm{H}_0^{(2)}(\kappa_1\rho_0) = \kappa_0\mathrm{J}_0(\kappa_0\rho_0) \\ a_1\epsilon_1\mathrm{H}_1^{(1)}(\kappa_1\rho_0) + b_1\epsilon_1\mathrm{H}_1^{(2)}(\kappa_1\rho_0) = \epsilon_0\mathrm{J}_1(\kappa_0\rho_0). \end{cases} \tag{3.18}$$

The equation (3.18) together with (3.10) and (3.11) represent an $(2N+2)\times(2N+1)$ overdetermined linear system of equations

$$\mathbf{B}\mathbf{x} = \mathbf{b} \tag{3.19}$$

where $\mathbf{x}$ is a vector containing the unknowns a_i and b_i for $i = 1, \ldots, N$ and b_{N+1}. The system (3.19) can be solved in a least squares sense using a pseudo-inverse [9, 14]. However, this is not sufficient when the problem is severely ill-conditioned. A Jacobi preconditioning [9, 14] is incorporated by instead solving the problem

$$\mathbf{B}\mathbf{D}^{-1/2}\mathbf{y} = \mathbf{b} \tag{3.20}$$

where $\mathbf{y} = \mathbf{D}^{1/2}\mathbf{x}$ and where $\mathbf{D}$ is a diagonal matrix with the same diagonal elements as the matrix $\mathbf{B}^{\mathrm{H}}\mathbf{B}$. The inversion of (3.20) is well-conditioned since the matrix $(\mathbf{B}\mathbf{D}^{-1/2})^{\mathrm{H}}\mathbf{B}\mathbf{D}^{-1/2}$ has unit diagonal.

The characteristic impedance is then finally obtained as

$$Z = \frac{V^+(z)}{I^+(z)}. \tag{3.21}$$

4 Experimental and numerical examples

4.1 Measurements and modeling for the HVDC power cable

A measurement campaign was pursued in June 2011 regarding time-domain measurements and modeling of an 80 km long 200 kV HVDC sea cable that was rolled up on shore, see Figure 4. The purpose was to evaluate the electromagnetic model that has been described in this paper.

Figure 4: An 80 km long 200 kV HVDC sea cable rolled up on shore.

The measurement set-up has been described in section 2 including an illustration of the connection between the extruded HVDC power cable and the measurement cable, see Figure 2. The measurement data was acquired using a 500 MHz sampling oscilloscope. The geometrical and electrical properties of the cable have been estimated based on data sheets and drawings as illustrated in Figure 5.

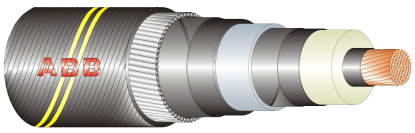

Figure 5: Cross-section of the extruded HVDC sea cable.

Layer	radius [mm]	permittivity	conductivity
Inner conductor	$\rho_0 = 24.3$	$\epsilon_{r0} = 1$	$\sigma_0 = \sigma_{Cu}$
Conductor screen	$\rho_1 = 26.0$	$\epsilon_{r1} = \epsilon_d$	$\sigma_1 = \sigma_s$
Insulation	$\rho_2 = 42.0$	$\epsilon_{r2} = \epsilon_d$	$\sigma_2 = 0$
Insulation screen	$\rho_3 = 43.9$	$\epsilon_{r3} = \epsilon_d$	$\sigma_3 = \sigma_s$
Lead sheat	$\rho_4 = 46.9$	$\epsilon_{r4} = 1$	$\sigma_4 = \sigma_{Pb}$
Inner sheat	$\rho_5 = 49.5$	$\epsilon_{r5} = \epsilon_d$	$\sigma_5 = 0$
Armour	$\rho_6 = 53.5$	$\epsilon_{r6} = 1$	$\sigma_6 = \sigma_{Fe}$
Outer serving	$\rho_7 = 58.5$	$\epsilon_{r7} = \epsilon_d$	$\sigma_7 = 0$
Exterior region	$\rho_8 = \infty$	$\epsilon_{r8} = (1, 80)$	$\sigma_8 = (0, 1)$

Table 1: Modeling parameters.

Due to the difficulty to determine the exact electrical properties of all layers, a simplified model has been used where we have incorporated the properties that we believe are the most significant, see Table 1. The permittivity of the insulation, the semi-conducting XLPE screens, the inner sheat and the outer serving are modeled with $\epsilon_{\rm d} = 2.3$. The conductivity of the semi-conducting XLPE screens are modeled with $\sigma_{\rm s} = 1\,{\rm S/m}$. The conductivity of the inner conductor, the lead sheat and the armour are modeled with $\sigma_{\rm Cu} = 5.8 \cdot 10^7\,{\rm S/m}$, $\sigma_{\rm Pb} = 4.6 \cdot 10^6\,{\rm S/m}$ and $\sigma_{\rm Fe} = 1.1 \cdot 10^6\,{\rm S/m}$, respectively. The permittivity of the exterior region is modeled either with $\epsilon_{\rm r8} = 1$ (air) or $\epsilon_{\rm r8} = 80$ (water), and the corresponding conductivity is either $\sigma_8 = 0$ (air) or $\sigma_8 = 1\,{\rm S/m}$ (sea-water).

Based on these modeling parameters, the electromagnetic model described in section 3 has been evaluated as described below. Unless otherwise stated, the cable is modeled with exterior parameters $\epsilon_{\rm r8} = 1$ and $\sigma_8 = 0$ (air). For the FFT calculations has been used $N = 16384$, and hence the propagation constant γ and the characteristic impedance Z have been calculated for $N/2 = 8192$ frequency points, as described in section 2 and 3, and in Appendix A. A time period $T = 0.08\,{\rm s}$ was chosen corresponding to a frequency sampling interval $\Delta f = 1/T = 12.5\,{\rm Hz}$, a sampling rate $f_{\rm s} = N\Delta f = 204.8\,{\rm kHz}$ and a sampling interval $T_{\rm s} = 1/f_{\rm s} = 4.88\,\mu{\rm s}$. Figure 6 illustrates the frequency domain windowing and the time domain resolution and dynamics corresponding to a modeling bandwidth of 102.4 kHz. A Kaiser window [11, 12, 21, 27] with parameter $\beta = 8$ has been used together with the IFFT operation in order to suppress the Gibbs phenomena in the time-domain, see also Appendix A.

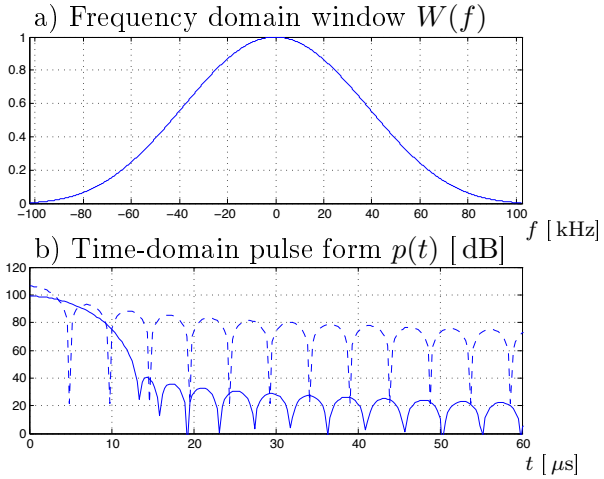

Figure 6: Illustration of frequency domain windowing and time-domain resolution and dynamics. The upper plot a) shows the Kaiser window with parameter $\beta = 8$ for a modeling bandwidth of 100 kHz. The lower plot b) shows a comparison between the convolving pulse form $p(t)$ (plotted here as $20\log|p(t)|$ in dB) obtained from the Kaiser window (solid line) and a rectangular window (dashed line).

The zero finding algorithm is based partly on a visual inspection of a two-dimensional plot of the dispersion function $\det \mathbf{A}(\gamma)$, as illustrated in Figures 7 and 8. The Figures 7 and 8 show the zeros corresponding to the quasi-TEM mode

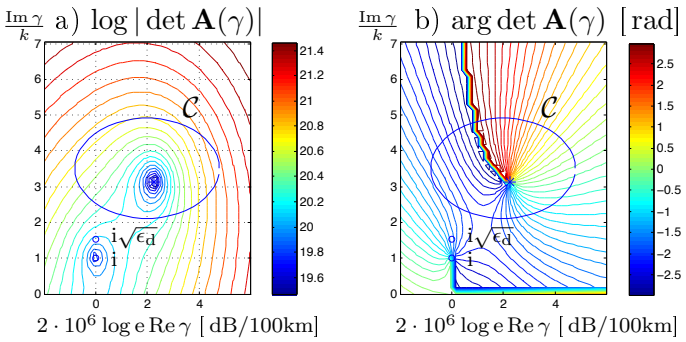

Figure 7: Illustration of a) amplitude and b) argument of the dispersion function $\det \mathbf{A}(\gamma)$ for $f = 50$ Hz and the quasi-TEM mode TM_{01}. The contour $\mathcal{C}$ is obtained (estimated) from the previous frequency (37.5 Hz) and is used to calculate the zero at the present frequency (50 Hz). The points $\gamma = \mathrm{i}k$ and $\gamma = \mathrm{i}k\sqrt{\epsilon_\mathrm{d}}$ are indicated with small circles.

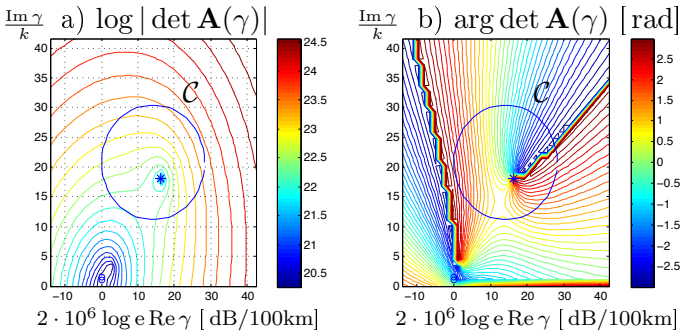

Figure 8: Illustration of a) amplitude and b) argument of the dispersion function $\det \mathbf{A}(\gamma)$ for $f = 50$ Hz and the second mode TM_{02}. The contour $\mathcal{C}$ is obtained (estimated) from the previous frequency (37.5 Hz) and is used to calculate the zero at the present frequency (50 Hz).

TM_{01} and the second mode TM_{02}, respectively. To this end, it is very useful to observe the TEM wave number $\mathrm{i}k\sqrt{\epsilon_\mathrm{d}}$ which approximates the dominating quasi-TEM mode TM_{01} and where ϵ_d is the permittivity of the insulating dielectric layer. It is also very useful to observe the point $\gamma = \mathrm{i}k\sqrt{\epsilon_{N+1}} = \mathrm{i}k$, where there is a branch-cut originating from the Hankel function representing the exterior domain. Given an estimate $\hat{\gamma}_1(k)$ of the propagation constant at wave number k, the contour $\mathcal{C}$ in (3.13) is defined here as an ellipse centered at $\hat{\gamma}_1(k)$ with x-radius $r2\,\mathrm{Re}\,\hat{\gamma}_1(k)$ and y-radius $r(\mathrm{Im}\,\hat{\gamma}_1(k) - k\sqrt{\epsilon_\mathrm{d}})$, which are assumed to be positive quantities. When the proportionality parameter r of the ellipse is less than 1 (here $r = 0.7$) this procedure guarantees that the branch-cut is avoided at $\gamma = \mathrm{i}k$. To determine an initial guess $\hat{\gamma}_1(k + \Delta k)$ at the new frequency point at $k + \Delta k$, it is assumed that $\mathrm{Im}\,\gamma_1(k)$ is approximately linear in k, yielding the formula $\hat{\gamma}_1(k + \Delta k) = \gamma_1(k) + \mathrm{i}\,\mathrm{Im}\,\gamma_1(k)\frac{\Delta k}{k}$.

Figure 9 illustrates a comparison between the time-domain measurement data

and the modeled response based on the quasi-TEM mode TM_{01}. The amplitude and the pulse-width of the transmitted rectangular pulse (2.7) was $V_{\mathrm{s}0} = 53\,\mathrm{V}$ and $T_{\mathrm{p}} = 98.6\,\mu\mathrm{s}$, respectively. The short spikes that are visible in the measurement data are due to the $50\,\Omega$ measurement coaxial cable with length $d_0 \approx 10\,\mathrm{m}$. As the power cable is placed on shore during the measurement, the cable is modeled with exterior parameters $\epsilon_{\mathrm{r}8} = 1$ and $\sigma_8 = 0$. Based on the electromagnetic model, the length of the HDVC power cable was estimated to $d = 82\,\mathrm{km}$.

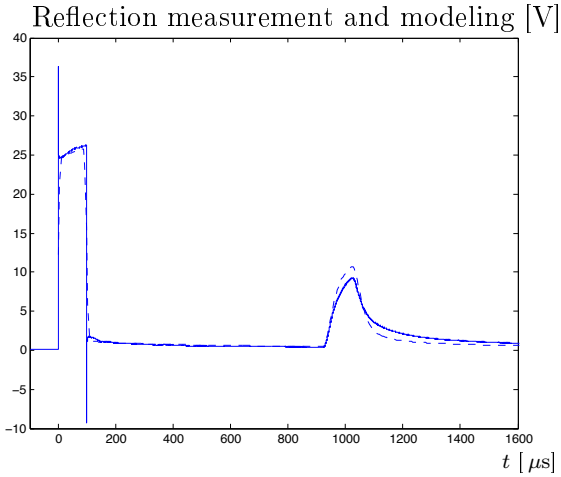

Figure 9: Comparison between measurement data (solid line) and modeled response (dashed line) based on the quasi-TEM mode TM_{01}. A rectangular pulse with duration $100\,\mu\mathrm{s}$ was transmitted at $t = 0$ and the reflected pulse was received at about $930\,\mu\mathrm{s}$.

The electromagnetic model can be used to investigate the low-frequency dispersion characteristics of the power cable and its dependence of various material and geometrical parameters. A few examples are given below. Figure 10 shows the normalized wave velocity and the attenuation due to the quasi-TEM mode TM_{01} over the frequency range 0–100 kHz. Figure 11 shows the normalized wave velocity and the attenuation for both the TM_{01} and the TM_{02} modes over the frequency range 0–1 kHz. Figure 12 shows the characteristic impedance for the TM_{01} and the TM_{02} modes over the frequency range 0–1 kHz. As can be seen in these figures, the TM_{02} mode is propagating, but is highly damped at higher frequencies. Hence, it is observed that the higher order modes may have an impact on the modeled response depending on their level of excitation.

As an illustration of a simple parameter study regarding the dominating quasi-TEM mode TM_{01}, the following three different cases are studied where the exterior domain is characterized by $(\epsilon_{\mathrm{r}8}, \sigma_8) = (1, 0)$ (air), $(\epsilon_{\mathrm{r}8}, \sigma_8) = (80, 0)$ (water) and $(\epsilon_{\mathrm{r}8}, \sigma_8) = (80, 1)$ (sea-water). The corresponding wave propagation characteristics over the frequency range 0–1 kHz are shown in Figures 13 and 14. This example suggests that the presence of the sea-water conductivity is noticeable only at the lower frequencies below 300-400 Hz, where there is a slight decrease in the attenuation and the imaginary part of the characteristic impedance changes significantly.

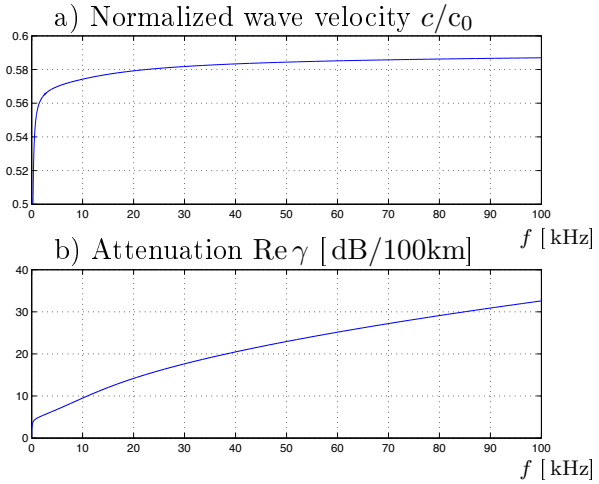

Figure 10: Low-frequency dispersion characteristics of the power cable over the frequency range 0–100 kHz based on the quasi-TEM mode TM_{01}: a) Normalized wave velocity $c/\mathrm{c}_0 = k/\operatorname{Im}\gamma(k)$. b) Attenuation $2 \cdot 10^6 \log \mathrm{e} \operatorname{Re}\gamma$ in dB/100km.

As was seen in Figure 9 above, there is a slight discrepancy between the measurement data and the modeled response based on the quasi-TEM mode TM_{01}. In particular, it seems that the electromagnetic model under-estimates the attenuation of the reflected pulse at early times and over-estimates the attenuation of the pulse at later times. Observe, however, that the agreement between the measurements and the model is best at very early times of pulse arrival at about 930–950 μs, indicating a difficulty to model correctly the propagation at lower frequencies.

4.2 Modeling based on mismatch calibration

To investigate the possibility to improve the model due to the excitation of higher order modes, a mismatch calibration has been performed as described in section 2.2. The resulting model (2.11) is then used in an example of high-resolution length-estimation as described below. The propagation constant γ corresponding to the TM_{01} mode is given by the electromagnetic model described in section 3.1. The cable is modeled here with the exterior parameters $\epsilon_{\mathrm{r}8} = 1$ and $\sigma_8 = 0$.

Two measurements based on reflection and transmission were conducted as illustrated in Figure 15. The excitation pulse amplitude $V_{\mathrm{s}0}$ was 53 V and 25 V, respectively, and the pulse time was about $T_{\mathrm{p}} = 100\,\mu$s in both cases. The measurement data was low-pass filtered and resampled to the sampling rate corresponding to the FFT computations as described in section 4.1 above ($f_{\mathrm{s}} = 204.8$ kHz). The data was also extrapolated to the full N-point FFT-grid by using the following model for the pulse tail

$$\frac{C}{\sqrt{(t-t_0)^3}} \tag{4.1}$$

where t_0 is the initial time of the pulse and C a constant. This model is motivated by the Laplace transform pair $s\frac{1}{\sqrt{s}}\mathrm{e}^{-A\sqrt{s}} \leftrightarrow \frac{\partial}{\partial t}\frac{1}{\sqrt{\pi t}}\mathrm{e}^{-A^2/4t}$ as a coarse model for the

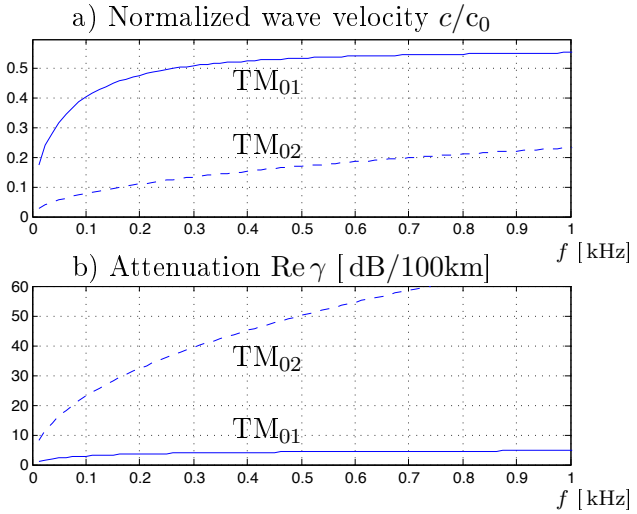

Figure 11: Low-frequency dispersion characteristics of the power cable over the frequency range 0–1 kHz: a) Normalized wave velocity $c/c_0 = k/\operatorname{Im}\gamma(k)$. b) Attenuation $2 \cdot 10^6 \log \mathrm{e} \operatorname{Re}\gamma$ in dB/100km. The solid lines show the TM_{01} mode and the dashed lines the TM_{02} mode.

transmission factor $S_{21}S_{12}\mathrm{e}^{-\gamma d}$ at late times. The reflection measurement data was finally time-gated.

After performing the FFT operation on the pre-processed measurement data shown in Figure 15, the estimated transmission coefficient $\widehat{S_{21}S_{12}}$ was computed as given by (2.10). Figure 16 shows a comparison between the magnitude of the transmission coefficient $|S_{21}S_{12}|$ obtained from the single-mode transmission line model as described in section 2.1, and the calibrated parameters as described in section 2.2. It is noted that the loss in transmission according to the calibrated parameters is expected due to the scattering of higher order modes.

Figure 17 shows a comparison between the transmission measurement data, the modeled response based on single-mode transmission line theory and the modeled response based on mismatch calibration (2.11). It is observed that the agreement between the measurements and the model is best at early times of pulse arrival. Based on an optimization over the raising edge of the measured pulse in the interval $460 - 560\,\mu$s (as indicated in Figure 17), the length of the power cable is estimated to $d = 81.8\,$km. The corresponding misfit functional is defined by

$$\mathcal{E}(d) = \frac{1}{t_1 - t_0} \int_{t_0}^{t_1} |v_{\mathrm{t}}^{\mathrm{M}}(t) - v_{\mathrm{t}}(t)|^2 \,\mathrm{d}t \tag{4.2}$$

where $[t_0, t_1]$ defines the optimization interval and $v_{\mathrm{t}}^{\mathrm{M}}(t)$ and $v_{\mathrm{t}}(t)$ denote the measured and modeled responses, respectively. The least square error $\mathcal{E}(d)$ and the optimal modeling error are illustrated in Figure 18. In Figure 19 is shown a comparison of the attenuation and the phase delay of the power cable based on the modeled transmission factor $\mathrm{e}^{-\gamma d}$ (with $d = 81.8\,$km) and the estimated $\widehat{\mathrm{e}^{-\gamma d}}$ given by (2.10).

It is concluded that a single-mode transmission line model is not adequate to account for the mismatch between the power cable and the instrumentation, and that

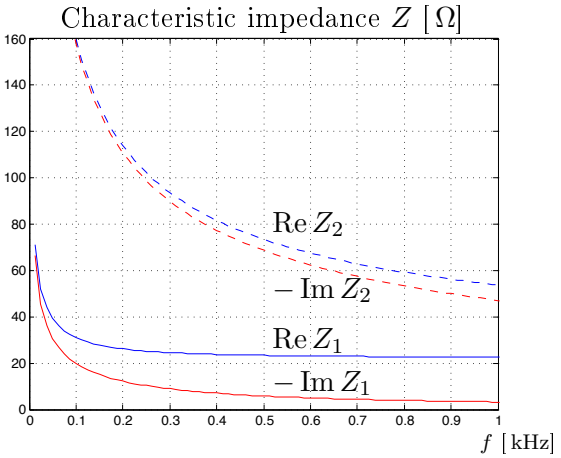

Figure 12: Low-frequency impedance characteristics of the power cable over the frequency range 0–1 kHz. The blue lines show $\mathrm{Re}\, Z$ and the red lines show $-\mathrm{Im}\, Z$ corresponding to the two modes TM_{01} (solid lines) and TM_{02} (dashed lines), respectively.

the mismatch calibration procedure yields a model that is accurate for early times of pulse arrival. There are several physical circumstances to consider to account for the remaining modeling errors. Possible candidates are *e.g.*, the choice of modeling parameters, the radius of curvature of the rolled up cable (here approximately 15-20 m) and the corresponding coupling, the presence of a continuous spectrum in the solution to the Maxwell's equations, the need for more elaborate modeling of the cable armour consisting of steel wires or the need to further improve the mismatch calibration and/or modeling to account for the connection between the power cable and the measurement cable. It is difficult to say which of the factors listed above that has the greatest impact on the modeling error, but we believe that the latter two are of great interest, *i.e.*, to incorporate into the model the effect of the cable armour and the excitation of higher order modes at the cable connection.

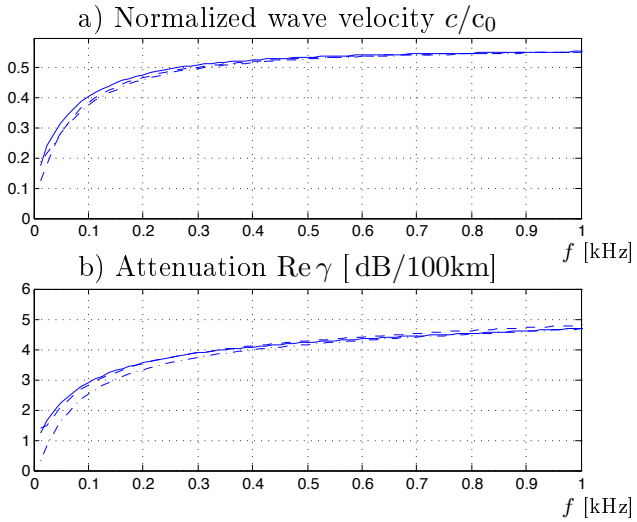

Figure 13: Parameter study with regard to the dispersion characteristics of the power cable TM_{01} mode over the frequency range 0–1 kHz: a) Normalized wave velocity $c/c_0 = k/\,\mathrm{Im}\,\gamma(k)$. b) Attenuation $2 \cdot 10^6 \log \mathrm{e}\,\mathrm{Re}\,\gamma$ in dB/100km. The exterior parameters are $(\epsilon_{\mathrm{r}8}, \sigma_8) = (1, 0)$ (solid lines), $(\epsilon_{\mathrm{r}8}, \sigma_8) = (80, 0)$ (dashed lines) and $(\epsilon_{\mathrm{r}8}, \sigma_8) = (80, 1)$ (dash-dotted lines).

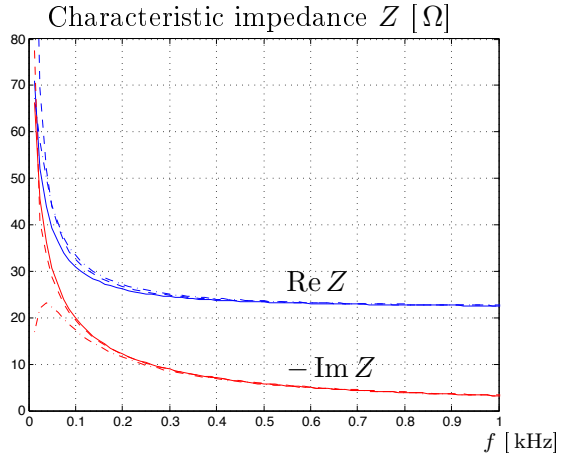

Figure 14: Parameter study with regard to the impedance characteristics of the power cable TM_{01} mode over the frequency range 0–1 kHz. The blue lines show $\mathrm{Re}\,Z$ and the red lines show $-\,\mathrm{Im}\,Z$. The exterior parameters are $(\epsilon_{\mathrm{r}8}, \sigma_8) = (1, 0)$ (solid lines), $(\epsilon_{\mathrm{r}8}, \sigma_8) = (80, 0)$ (dashed lines) and $(\epsilon_{\mathrm{r}8}, \sigma_8) = (80, 1)$ (dash-dotted lines).

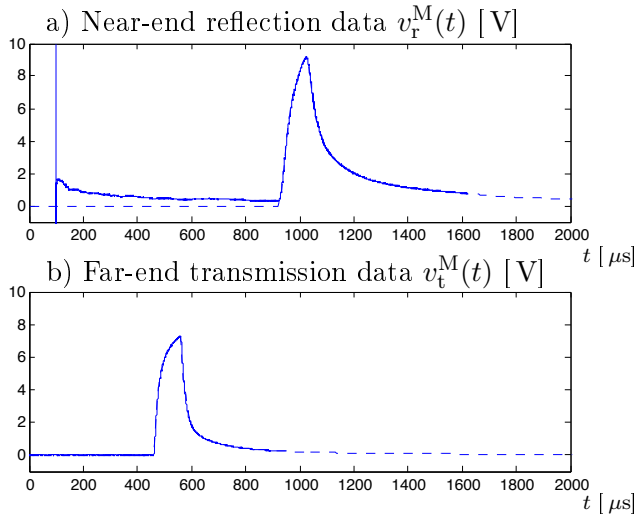

Figure 15: Input data for mismatch calibration: a) reflection data. b) transmission data. The solid lines show the original measurement data and the dashed lines the resampled and extrapolated data. The reflection data has been time-gated.

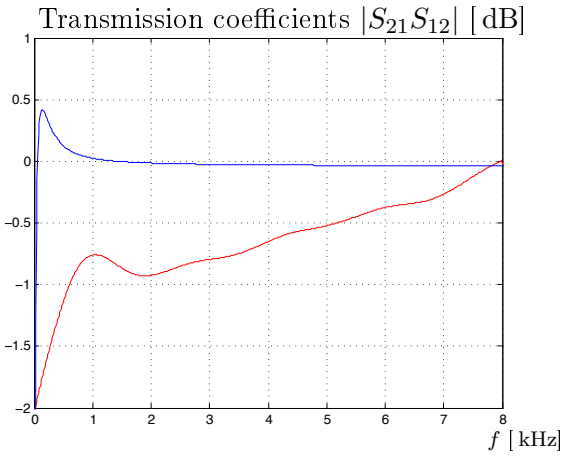

Figure 16: Magnitude of the transmission coefficients $|S_{21}S_{12}|$. The blue line is based on the single-mode transmission line model and the red line on the calibrated parameters.

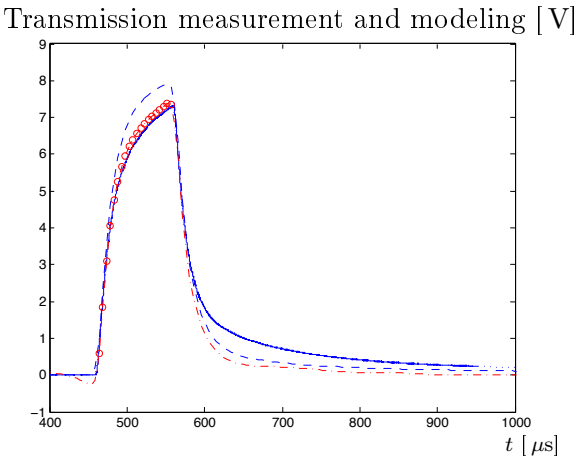

Figure 17: Comparison between transmission measurement data (solid line), modeled response based on single-mode transmission line theory (dashed line) and modeled response based on mismatch calibration (red dash-dotted line). A rectangular pulse with duration $100\,\mu$s was transmitted at $t = 0$ and received at the far-end at about $460\,\mu$s. The time-domain samples for length-estimation are based on the raising edge of the measured pulse in the interval $460 - 560\,\mu$s, and the corresponding modeled response is indicated here by the red circles.

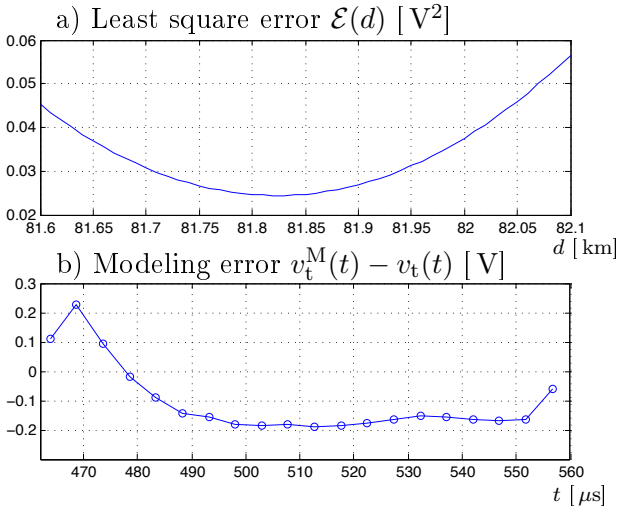

Figure 18: a) Least square error $\mathcal{E}(d)$ as a function of estimated distance d. b) Modeling error for $d = 81.8\,$km.

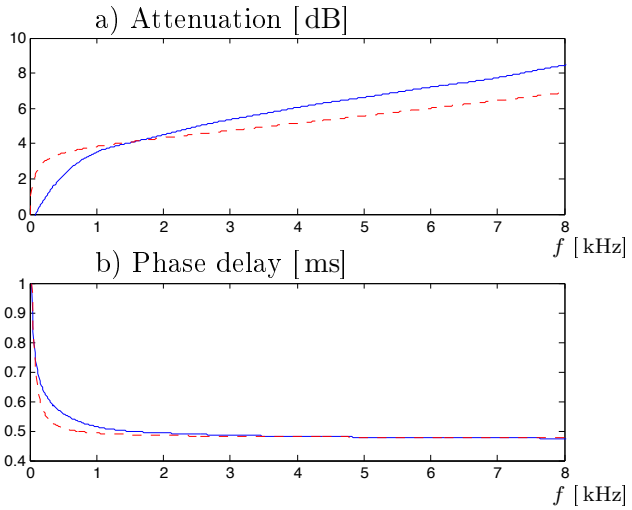

Figure 19: a) Attenuation $\mathrm{Re}\,\gamma d \cdot 20 \log \mathrm{e}$ in dB. b) Phase delay $\mathrm{Im}\,\gamma d/\omega$ in ms. The length is estimated to $d = 81.8\,\mathrm{km}$. The solid blue lines show the measured quantities based on the mismatch calibration and the red dashed lines the corresponding modeled quantities.

4.3 Statistical sensitivity analysis for high-resolution length-estimation

To illustrate the potential of high-resolution distance measurements for very long power cables, a statistically based sensitivity analysis is described below. Hence, based on the assumption that the measurement noise is uncorrelated and Gaussian distributed, in addition to the assumption that the electromagnetic model given by (2.4) in section 2 is perfectly correct, the Cramér-Rao lower bound [13, 31] for estimating the distance parameter d can be readily calculated. The basic definitions and derivations regarding the maximum likelihood criterion and the Fisher information for measurements over a frequency interval can be found in *e.g.*, [15, 18].

If the assumptions stated above are fulfilled, the maximum likelihood criterion [13, 31] for estimating d is based on the least squares error functional

$$\int_{-\infty}^{\infty} |v^{\mathrm{M}}(t) - v(t,d)|^2 \,\mathrm{d}t = \int_{-\infty}^{\infty} |V^{\mathrm{M}}(f) - V(f,d)|^2 \,\mathrm{d}f \tag{4.3}$$

where $v^{\mathrm{M}}(t)$ and $V^{\mathrm{M}}(f)$ represent the measured voltages and $v(t,d)$ and $V(f,d)$ the modeled voltages in the time and frequency domains, respectively. Furthermore, the Fisher information [13, 31] for the distance parameter d based on an observation over the frequency interval $[-B, B]$, is given by

$$\mathcal{I}(d) = \int_{-B}^{B} \frac{1}{R_N(f)} \left| \frac{\partial V}{\partial d} \right|^2 \mathrm{d}f = \frac{1}{N_0} \int_{-B}^{B} 4 \left| \gamma V_0^+ S_{21} S_{12} \mathrm{e}^{-2\gamma d} \right|^2 \mathrm{d}f, \tag{4.4}$$

where $R_N(f)$ is the power spectral density [26] of the noise. Here, it has been assumed that the power spectral density is a constant N_0 over the frequency interval of interest and $\frac{\partial V}{\partial d} = -2\gamma V_0^+ S_{21} S_{12} \mathrm{e}^{-2\gamma d}$ has been used based on the model given by (2.4) and (2.5) in section 2. The Cramér-Rao lower bound [13, 31] asserts that the error variance of any unbiased estimator $\hat{d}$ of the parameter d is lower bounded by $\mathrm{Var}\{\hat{d}\} \geq 1/\mathcal{I}(d)$. Hence, a statistically based measure of the best possible accuracy (which is also asymptotically achievable [13, 31]), is given by the corresponding standard deviation $1/\sqrt{\mathcal{I}(d)}$.

To validate the first assumption above, a normal probability plot [6] was made based on measurement noise that was collected prior to pulse excitation, see Figure 20. The measurement set-up and parameter choices were the same as have been described in the previous sections and illustrated in Figure 9. A record of noise over a 375 μs interval at a sampling rate of 500 MHz was analyzed, and the power spectral density of the noise was estimated to $N_0 = 2.1 \cdot 10^{-13}\,\mathrm{V^2s}$. The normal probability plot was obtained by using the statistics toolbox in Matlab, and it shows a very close linear fit with respect to the normal distribution. This is a clear indication that the normal (or Gaussian) assumption about the noise statistics is well justified, see [6]. A spectrum analysis also revealed that the noise can be regarded to be uncorrelated over the frequency interval of interest.

Assuming that the electromagnetic model is perfectly correct, the corresponding statistical accuracy $1/\sqrt{\mathcal{I}(d)}$ is obtained using (4.4). Figures 21 a) and b) show

the statistical accuracy as a function of the measurement bandwidth B over the frequency ranges 0–500 Hz and 0–50 kHz, respectively. These plots illustrate the potential of achieving high-resolution estimation performance based on an extremely accurate electromagnetic model, where the model errors can be neglected in comparison to the measurement errors. Based on the analysis of the measurement noise in this particular example, a length-estimation accuracy in the order of centimeters would be possible for a cable with a total length in the order of 10–80 km.

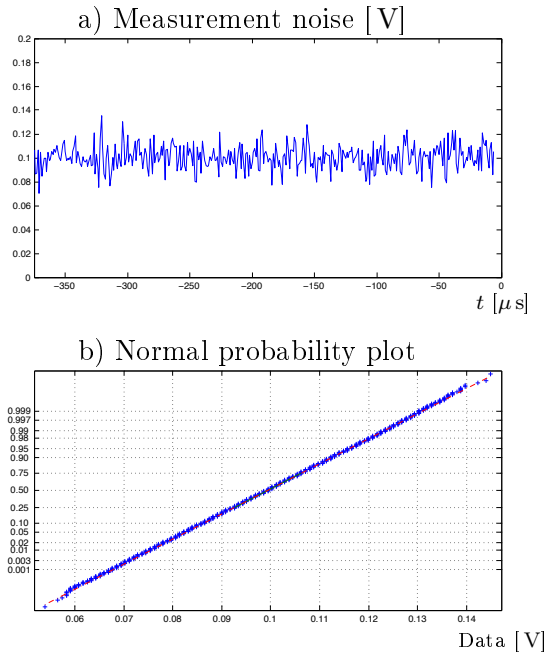

Figure 20: Illustration of measurement noise statistics. The upper plot a) shows 375 μs of the measurement noise prior to pulse excitation (decimated here to a sampling rate of 1 MHz). The lower plot b) shows a normal probability plot corresponding to 375 μs of the measurement noise at a sampling rate of 500 MHz (187500 data points).

4.4 Statistical sensitivity analysis based on mismatch calibration

A Fisher information analysis is given below regarding the high-resolution length-estimation based on mismatch calibration, as described in section 4.2. The modeled response V_t is given by (2.11) where the propagation constant γ is modeled as described in section 3.1. The misfit functional for length-estimation is given by (4.2). The Fisher information for length-estimation based on the finite time interval $[t_0, t_1]$

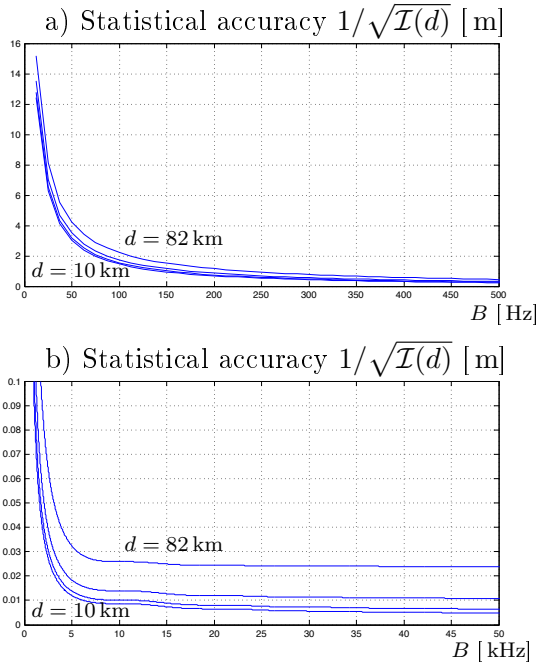

Figure 21: Illustration of the potential of high-resolution estimation. The upper plot a) shows the statistical accuracy $1/\sqrt{\mathcal{I}(d)}$ over the frequency range $0-500\,\mathrm{Hz}$. The lower plot b) shows the statistical accuracy $1/\sqrt{\mathcal{I}(d)}$ over the frequency range $0-50\,\mathrm{kHz}$. In both cases, four plots are shown for $d = 10, 20, 41, 82\,\mathrm{km}$.

is given by[4]

$$\mathcal{I}(d) = \frac{1}{N_0}\int_{t_0}^{t_1}\left|\frac{\partial v_\mathrm{t}(t)}{\partial d}\right|^2 \mathrm{d}t \approx \frac{T_\mathrm{s}}{N_0}\sum_i \left|\frac{\partial v_\mathrm{t}(t_i)}{\partial d}\right|^2 \tag{4.5}$$

where N_0 is the spectral density of the noise and the sensitivity pulse $\frac{\partial v_\mathrm{t}(t)}{\partial d}$ is the inverse Fourier transform of the corresponding sensitivity expression in the frequency domain

$$\frac{\partial V_\mathrm{t}}{\partial d} = -\gamma V_{0\mathrm{t}}^{+}\widehat{S_{21}S_{12}}\mathrm{e}^{-\gamma d}. \tag{4.6}$$

The sensitivity pulse $\frac{\partial v_\mathrm{t}(t)}{\partial d}$ is readily computed from an inverse FFT operation based on (4.6) and is plotted in Figure 22.

Let the Noise-Ratio NR be defined by $\mathrm{NR} = N_0/(2.1\cdot 10^{-13})$ in relation to the noise level of the present measurement data. Figure 23 shows the statistical accuracy $1/\sqrt{\mathcal{I}(d)}$ based on (4.5) as a function of the noise ratio NR. Assuming that there is no modeling error, it is seen from Figure 23 that the estimation accuracy for $\mathrm{NR} = 0\,\mathrm{dB}$ is in the order of centimeters. In Figure 23, the vertical dashed line indicates the noise ratio that corresponds to the modeling error, *i.e.*, $\mathrm{NR} = \mathcal{E}(d)T_\mathrm{s}/(2.1\cdot 10^{-13}) = 57.6\,\mathrm{dB}$ where $\mathcal{E}(d)$ is given by (4.2), see also Figure 18.

[4]The time-domain expression (4.5) follows readily from (4.4) by an application of the Parseval's relation.

When the noise ratio is significantly above this limit, the model error is much less than the Gaussian noise and can hence be neglected. It is therefore concluded from Figure 23 that the accuracy for length-estimation in this application example is in the order of 100 m.

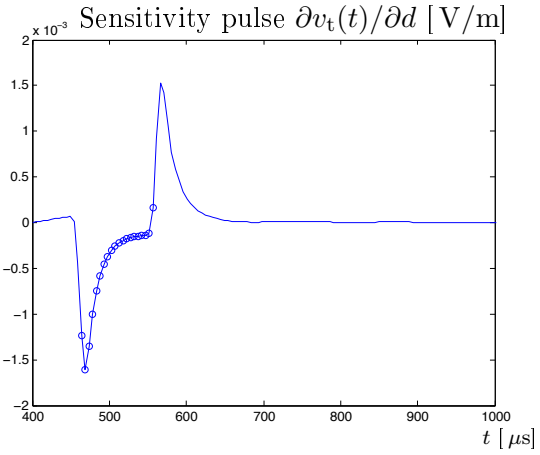

Figure 22: The sensitivity pulse $\partial v_{\mathrm{t}}(t)/\partial d$. The time-domain samples for length-estimation are based on the raising edge of the measured pulse in the interval $460-560\,\mu$s, and the corresponding sensitivity values are indicated here by the blue circles.

5 Summary and future work

A general framework for electromagnetic modeling and computation regarding the wave propagation characteristics of HVDC power cables has been presented in this paper. The computational framework is well suited for time- and/or frequency-domain measurements and modeling for very long (10 km or more) HVDC power cables in the low frequency regime of about 0–100 kHz. An exact dispersion relation is formulated together with a discussion on practical aspects regarding the computation of the propagation constant and the related characteristic impedance. Experimental time-domain measurement data from an 80 km long HVDC power cable is used to validate the model. It is concluded that a single-mode transmission line model is not adequate to account for the mismatch between the power cable and the instrumentation. A mismatch calibration procedure is therefore devised to account for the connection between the measurement equipment and the cable. A dispersion model is thus obtained that is accurate for early times of pulse arrival.

It is anticipated that an "exact" electromagnetic model will potentially be very useful for future fault localization and diagnosis systems regarding the surveillance of very long HVDC power cables, as well as for the possibility to measure accurately the length of the power cables as an aid in the manufacturing process. Hence, future work will be devoted to improve the electromagnetic dispersion models with the aim of reaching an "exact" agreement between the measurement data and the modeling in the sense that the modeling errors are less than (or comparable to) the measurement

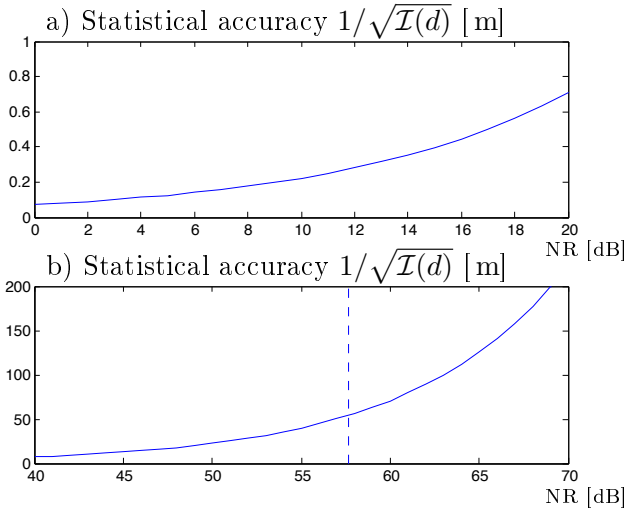

Figure 23: a) Statistical accuracy $1/\sqrt{\mathcal{I}(d)}$ over the Noise-Ratio interval $0-20\,\mathrm{dB}$. b) Statistical accuracy $1/\sqrt{\mathcal{I}(d)}$ over the Noise-Ratio interval $40-70\,\mathrm{dB}$. The computations are based on the estimated length $d = 81.8\,\mathrm{km}$. The vertical dashed line indicates where the noise ratio corresponds to the modeling error.

errors. To this end, a systematic study will be pursued in order to investigate the significance (*i.e.*, the sensitivity) of various modeling parameters. Possible model improvements such as the incorporation of the cable armour consisting of steel wires, or the connection to the power cable and the related excitation of higher order modes will also be investigated. It has also been observed that the agreement between the measurements and the model is best at very early times of pulse arrival, indicating a difficulty to model correctly the propagation at lower frequencies. Hence, it is also anticipated that there is a potential for developing asymptotic methods and electromagnetic models that are accurate for early times of pulse arrival, and to derive high-resolution estimation algorithms based on such models.

Acknowledgements

The research leading to these results has received funding from the Swedish Research Council as well as from ABB AB. The authors are also grateful to ABB AB for providing the opportunity to perform the cable measurements on their premises.

Appendix A Fast Fourier inversion and rejection of the Gibbs phenomena in the time-domain

The N-point Discrete Fourier Transform (DFT) and its inverse (IDFT) are defined by

$$\left\{ \begin{array}{rcl} S(k) & = & \displaystyle\sum_{n=0}^{N-1} s(n) \mathrm{e}^{-\mathrm{i}\frac{2\pi}{N}kn} \\ s(n) & = & \displaystyle\frac{1}{N} \sum_{k=0}^{N-1} S(k) \mathrm{e}^{\mathrm{i}\frac{2\pi}{N}kn} \end{array} \right. \tag{A.1}$$

where $s(n)$ is a real, discrete-time signal defined for $n = 0, 1, \ldots, N-1$ [21, 27]. An important property is that the symmetry $S(k) = S^*(N-k)$ holds if and only if $s(n)$ is real. Both signals $S(k)$ and $s(n)$ are regarded to be periodic with period N. An efficient algorithm to compute the DFT is the Fast Fourier Transform (FFT) where N is assumed to be a power of two, see *e.g.*, [21, 27].

Let $V(f) = \mathcal{F}v(t)$ denoted a frequency domain function which is observed over the frequency interval $f \in [-B, B]$ where B is the bandwidth. Here, $\mathcal{F}$ denotes the classical Fourier transform for continuous-time signals [23]. It is desired to employ the FFT to obtain an approximation of the inverse $v(t) = \mathcal{F}^{-1}V(f)$, based on N uniform samples of $V(f)$ over the bandwidth $f \in [-B, B]$.

Define the

$$\left\{ \begin{array}{l} \text{sampling rate: } f_\mathrm{s} = 2B \\ \text{samling interval: } T_\mathrm{s} = \frac{1}{f_\mathrm{s}} \\ \text{period: } T = NT_\mathrm{s} \\ \text{frequency sampling interval: } \Delta f = \frac{1}{T} = \frac{f_\mathrm{s}}{N} \end{array} \right. \tag{A.2}$$

and define the frequency domain samples by

$$\left\{ \begin{array}{rcll} S(k) & = & W_k V(f_k) & 0 \le k \le \frac{N}{2} - 1 \\ S(k) & = & 0 & k = \frac{N}{2} \\ S(k) & = & S^*(N-k) & \frac{N}{2} + 1 \le k \le N - 1 \end{array} \right. \tag{A.3}$$

where W_k is a positive window function, and where

$$f_k = k\Delta f. \tag{A.4}$$

The window function W_k is defined for $k = -\frac{N}{2} + 1, \ldots, \frac{N}{2} - 1$ and is symmetric with $W_k = W_{-k}$. The corresponding T-periodic time domain pulse is obtained as the following Fourier series

$$p(t) = \sum_{k=-\frac{N}{2}+1}^{\frac{N}{2}-1} W_k \mathrm{e}^{\mathrm{i}\frac{2\pi}{T}kt}. \tag{A.5}$$

Define also the Fourier series coefficients

$$S_\mathrm{p}(k) = \left\{ \begin{array}{ll} \frac{1}{T} S(k) & -\frac{N}{2} + 1 \le k \le \frac{N}{2} - 1 \\ 0 & |k| \ge \frac{N}{2} \end{array} \right. \tag{A.6}$$

and the corresponding T-periodic function

$$s_{\mathrm{p}}(t) = \sum_{k=-\frac{N}{2}+1}^{\frac{N}{2}-1} S_{\mathrm{p}}(k)\mathrm{e}^{\mathrm{i}\frac{2\pi}{T}kt}. \tag{A.7}$$

It is then readily seen that

$$\begin{aligned} s(n) = \frac{1}{N}\sum_{k=0}^{N-1} S(k)\mathrm{e}^{\mathrm{i}\frac{2\pi}{N}kn} = \frac{1}{N}\sum_{k=-\frac{N}{2}+1}^{\frac{N}{2}-1} TS_{\mathrm{p}}(k)\mathrm{e}^{\mathrm{i}\frac{2\pi}{N}kn} \\ = T_{\mathrm{s}}\sum_{k=-\frac{N}{2}+1}^{\frac{N}{2}-1} S_{\mathrm{p}}(k)\mathrm{e}^{\mathrm{i}\frac{2\pi}{T}knT_{\mathrm{s}}} = T_{\mathrm{s}}s_{\mathrm{p}}(nT_{\mathrm{s}}), \end{aligned} \tag{A.8}$$

and hence

$$s_{\mathrm{p}}(nT_{\mathrm{s}}) = \frac{1}{T_{\mathrm{s}}}s(n). \tag{A.9}$$

From (A.3) and (A.6) follows that

$$S_{\mathrm{p}}(k) = \frac{1}{T}V(f_k)W_k \tag{A.10}$$

and hence that

$$s_{\mathrm{p}}(t) = \frac{1}{T}\mathcal{P}\{v(t)\} \otimes p(t) \tag{A.11}$$

where $\otimes$ denotes the circular convolution defined by $x(t)\otimes y(t) = \int_T x(\tau)y(t-\tau)\,\mathrm{d}\tau$, and $\mathcal{P}\{v(t)\}$ the periodic extension

$$\mathcal{P}\{v(t)\} = \sum_{l=-\infty}^{\infty} v(t - lT) \tag{A.12}$$

with Fourier coefficients

$$\frac{1}{T}\int_T \mathcal{P}\{v(t)\}\mathrm{e}^{-\mathrm{i}\frac{2\pi}{T}kt}\,\mathrm{d}t = \frac{1}{T}V(f_k). \tag{A.13}$$

The window function W_k is chosen such that $W_0 = 1$, and $W_k \to 1$ for any fixed k as $N \to \infty$ and $T = NT_{\mathrm{s}}$ is fixed. Hence, the pulse $\frac{1}{T}p(t)$ approaches the periodic distribution

$$\frac{1}{T}p(t) \to \sum_{l=-\infty}^{\infty} \delta(t - lT), \tag{A.14}$$

and it follows from (A.11) that

$$s_{\mathrm{p}}(t) \to \sum_{l=-\infty}^{\infty} v(t - lT) \tag{A.15}$$

as $N \to \infty$ and $T = NT_{\mathrm{s}}$ is fixed. This is of course the reasonable asymptotic behavior of any well balanced window function.

Note that the relation (A.11) also displays the fact that with a finite window length N, it will be the main-lobe and the side-lobe behavior of the convolving pulse $p(t)$ that governs the time-domain resolution as well as the dynamic range and the effect of the Gibbs phenomena. To this end, the Kaiser window [11, 12, 21, 27] is a flexible window that can be used to trade time resolution (width of main-lobe) for dynamic range, *i.e.*, the rejection of side-lobes and the Gibbs phenomena in the time-domain.

Appendix B Cylindrical vector waves

The cylindrical vector waves are defined here by

$$\begin{cases} \boldsymbol{\chi}_{1m} = \dfrac{1}{\kappa}\nabla \times (\hat{\boldsymbol{z}}\psi_m(\kappa\rho)\mathrm{e}^{\mathrm{i}m\phi}\mathrm{e}^{-\gamma z}) \\ \boldsymbol{\chi}_{2m} = \dfrac{1}{k}\nabla \times \boldsymbol{\chi}_{1m} \end{cases} \tag{B.1}$$

where $\kappa = \sqrt{k^2\epsilon + \gamma^2}$ is the radial wave number with $\mathrm{Im}\,\kappa \leq 0$, and $\psi_m(\kappa\rho)\mathrm{e}^{\mathrm{i}m\phi}\mathrm{e}^{-\gamma z}$ is a scalar partial wave satisfying Helmholtz wave equation where $\psi_m(\kappa\rho)$ is a Bessel function or a Hankel function of the first or second kind and order m, see also [4, 10]. The scaling factors used in (B.1) can be defined differently, but are chosen here for notational convenience in the derivation of boundary conditions and dispersion relations. Note that the vector waves defined above are dimensionless.

The following explicit expressions are obtained in cylindrical coordinates

$$\begin{cases} \boldsymbol{\chi}_{1m}(\rho) = \hat{\boldsymbol{\rho}}\dfrac{\mathrm{i}m}{\kappa\rho}\psi_m(\kappa\rho) - \hat{\boldsymbol{\phi}}\psi_m'(\kappa\rho) \\ \boldsymbol{\chi}_{2m}(\rho) = -\hat{\boldsymbol{\rho}}\dfrac{\gamma}{k}\psi_m'(\kappa\rho) - \hat{\boldsymbol{\phi}}\dfrac{\mathrm{i}m\gamma}{k\kappa\rho}\psi_m(\kappa\rho) + \hat{\boldsymbol{z}}\dfrac{\kappa}{k}\psi_m(\kappa\rho) \end{cases} \tag{B.2}$$

where $\boldsymbol{\chi}_{lm} = \boldsymbol{\chi}_{lm}(\rho)\mathrm{e}^{\mathrm{i}m\phi}\mathrm{e}^{-\gamma z}$ $(l = 1, 2)$ and where $\psi'(\cdot)$ denotes a differentiation with respect to the argument.

It can be shown by direct calculation that $\nabla \times \boldsymbol{\chi}_{2m} = k\epsilon\boldsymbol{\chi}_{1m}$, and the following important curl properties are thus obtained

$$\begin{cases} \nabla \times \boldsymbol{\chi}_{1m} = k\boldsymbol{\chi}_{2m} \\ \nabla \times \boldsymbol{\chi}_{2m} = k\epsilon\boldsymbol{\chi}_{1m}. \end{cases} \tag{B.3}$$

It follows from (B.3) that the two cylindrical vector waves are source free with $\nabla \cdot \boldsymbol{\chi}_{1m} = \nabla \cdot \boldsymbol{\chi}_{2m} = 0$. Hence, the cylindrical vector waves satisfy also the vector Helmholtz wave equation

$$\begin{cases} \nabla^2\boldsymbol{\chi}_{1m} + k^2\epsilon\boldsymbol{\chi}_{1m} = \mathbf{0} \\ \nabla^2\boldsymbol{\chi}_{2m} + k^2\epsilon\boldsymbol{\chi}_{2m} = \mathbf{0} \end{cases} \tag{B.4}$$

and can therefore be used as models for solving the source-free Maxwell's equations (3.1).

The electric and magnetic fields can generally be expanded as

$$\boldsymbol{E} = \frac{1}{2\pi \mathrm{i}} \int_{-\mathrm{i}\infty}^{\mathrm{i}\infty} \left[\sum_{m=-\infty}^{\infty} a_{1m} \boldsymbol{\chi}_{1m}^{(1)} + b_{1m} \boldsymbol{\chi}_{1m}^{(2)} + a_{2m} \boldsymbol{\chi}_{2m}^{(1)} + b_{2m} \boldsymbol{\chi}_{2m}^{(2)} \right] \mathrm{d}\gamma \tag{B.5}$$

and

$$\boldsymbol{H} = \frac{1}{2\pi \eta_0} \int_{-\mathrm{i}\infty}^{\mathrm{i}\infty} \left[\sum_{m=-\infty}^{\infty} a_{1m} \boldsymbol{\chi}_{2m}^{(1)} + b_{1m} \boldsymbol{\chi}_{2m}^{(2)} + a_{2m} \epsilon \boldsymbol{\chi}_{1m}^{(1)} + b_{2m} \epsilon \boldsymbol{\chi}_{1m}^{(2)} \right] \mathrm{d}\gamma, \tag{B.6}$$

where $\boldsymbol{H} = \frac{1}{-\mathrm{i}\omega\mu_0} \nabla \times \boldsymbol{E}$ and (B.3) have been used, see also [4]. Here, a_{1m}, b_{1m}, a_{2m} and b_{2m} are complex valued expansion coefficients with the same dimension as the electric field (V/m), and which can be determined by applying the appropriate boundary conditions. The expansion (B.5) and (B.6) is valid in source free cylindrical regions or layers where the material parameter ϵ is constant. The vector waves $\boldsymbol{\chi}_{1m}^{(j)}$ and $\boldsymbol{\chi}_{2m}^{(j)}$ are based on Bessel functions or Hankel functions $\psi_m^{(j)}(\kappa\rho)$ of the first kind ($j = 1$) and the second kind ($j = 2$) denoted here by $\mathrm{J}_m(\kappa\rho)$ and $\mathrm{Y}_m(\kappa\rho)$, or $\mathrm{H}_m^{(1)}(\kappa\rho)$ and $\mathrm{H}_m^{(2)}(\kappa\rho)$, respectively, all of order m, see *e.g.*, [20].

For a homogeneous inner region the Neumann functions $\mathrm{Y}_m(\kappa\rho)$ become singular at $\rho = 0$, and hence only the Bessel functions of the first kind $\mathrm{J}_m(\kappa\rho)$ can be employed which are regular at the origin $\rho = 0$. For an unbounded outer domain, the Hankel function $\psi_m^{(2)}(\kappa\rho) = \mathrm{H}_m^{(2)}(\kappa\rho)$ of the second kind and order m is employed. This function satisfies the proper radiation condition [10] at infinity with $\mathrm{H}_m^{(2)}(\kappa\rho) \sim \sqrt{2/(\pi\kappa\rho)} \mathrm{e}^{-\mathrm{i}(\kappa\rho - m\pi/2 - \pi/4)}$ as $\rho \to \infty$, and $\lim_{\rho\to\infty} \mathrm{H}_m^{(2)}(\kappa\rho) = 0$ when $\mathrm{Im}\{\kappa\} \leq 0$. Note also that $\mathrm{H}_m^{(1)}(\kappa\rho)$ and $\mathrm{H}_m^{(2)}(\kappa\rho)$ can be interpreted as *incoming* and *outgoing* waves, respectively, when the time-convention is $\mathrm{e}^{\mathrm{i}\omega t}$.

References

[1] N. Amekawa, N. Nagaoka, and Y. Baba. Derivation of a semiconducting layer impedance and its effect on wave propagation characteristics on a cable. *IEE Proceedings – Generation, Transmission & Distribution*, **150**(4), 434–441, 2003.

[2] Z. Q. Bo. Transient based protection for power transmission system. In *IEEE Power Engineering Society Winter Meeting*, volume 3, pages 1832–1837, 2000.

[3] S. Boggs, A. Pathak, and P. Walker. Partial discharge. XXII. High frequency attenuation in shielded solid dielectric power cable and implications thereof for PD location. *IEEE Electrical Insulation Magazine*, **12**(1), 9–16, 1996.

[4] A. Boström, G. Kristensson, and S. Ström. Transformation properties of plane, spherical and cylindrical scalar and vector wave functions. In V. V. Varadan, A. Lakhtakia, and V. K. Varadan, editors, *Field Representations and Introduction to Scattering*, Acoustic, Electromagnetic and Elastic Wave Scattering, chapter 4, pages 165–210. Elsevier Science Publishers, Amsterdam, 1991.

[5] J. R. Carson and J. J. Gilbert. Transmission characteristic of the submarine cable. *Journal of the Franklin Institute*, **192**(6), 705–735, 1921.

[6] J. Chambers, W. Cleveland, B. Kleiner, and P. Tukey. *Graphical Methods for Data Analysis*. Wadsworth, 1983.

[7] R. E. Collin. *Field Theory of Guided Waves*. IEEE Press, New York, second edition, 1991.

[8] F. E. Gardiol. *Lossy transmission lines*. Artech House, Boston, London, 1987.

[9] A. Greenbaum. *Iterative Methods for Solving Linear Systems*. SIAM Press, Philadelphia, 1997.

[10] J. D. Jackson. *Classical Electrodynamics*. John Wiley & Sons, New York, third edition, 1999.

[11] J. F. Kaiser. Nonrecursive digital filter design using the Io-sinh window function. In *Proc. 1974 IEEE Symp. Circuits and Systems, (April 1974)*, pages 20–23, 1974.

[12] J. F. Kaiser and R. W. Schafer. On the use of the Io-sinh window for spectrum analysis. *IEEE Trans. Acoust., Speech, and Signal Processing*, **28**(1), 105–107, 1980.

[13] S. M. Kay. *Fundamentals of Statistical Signal Processing, Estimation Theory*. Prentice-Hall, Inc., NJ, 1993.

[14] C. T. Kelley. *Iterative Methods for Linear and Nonlinear Equations*. SIAM Press, Philadelphia, 1995.

[15] C. H. Knapp and G. C. Carter. The generalized correlation method for estimation of time delay. *IEEE Trans. Acoustics, Speech, and Signal Process.*, **ASSP-24**(4), 320–327, 1976.

[16] J. Lundbäck, S. Nordebo, and T. Biro. A digital directional coupler with applications to partial discharge measurements. *IEEE Transactions on Instrumentation and Measurements*, **57**(11), 2561–2567, 2008.

[17] J. Lundstedt. Condition for distortionfree transmission lines with a nonuniform characteristic impedance. *IEEE Trans. Microwave Theory Tech.*, **43**(6), 1386–1389, 1995.

[18] S. Nordebo, A. Fhager, M. Gustafsson, and B. Nilsson. A Green's function approach to Fisher information analysis and preconditioning in microwave tomography. *Inverse Problems in Science and Engineering*, **18**(8), 1043–1063, 2010.

[19] S. Nordebo, B. Nilsson, T. Biro, G. Cinar, M. Gustafsson, S. Gustafsson, A. Karlsson, and M. Sjöberg. Low-frequency dispersion characteristics of the multi-layered coaxial cable. Technical Report LUTEDX/(TEAT-7212)/1–21/(2011), Lund University, Department of Electrical and Information Technology, P.O. Box 118, S-221 00 Lund, Sweden, 2011. http://www.eit.lth.se.

[20] F. W. J. Olver, D. W. Lozier, R. F. Boisvert, and C. W. Clark. *NIST Handbook of mathematical functions*. Cambridge University Press, New York, 2010.

[21] A. V. Oppenheim and R. W. Schafer. *Discrete-time signal processing*. Signal processing series. Prentice-Hall, Inc., 1999.

[22] R. Papazyan, P. Pettersson, and D. Pommerenke. Wave propagation on power cables with special regard to metallic screen design. *IEEE Transactions on Dielectrics and Electrical Insulation*, **14**(2), 409–416, 2007.

[23] A. Papoulis. *The Fourier integral and its applications*. McGraw-Hill, Inc., New York, 1962.

[24] D. Pommerenke, T. Strehl, R. Heinrich, W. Kalkner, F. Schmidt, and W. Weissenberg. Discrimination between interal PD and other pulses using directional coupling sensors on HV cable systems. *IEEE Transactions on Dielectrics and Electrical Insulation*, **6**(6), 814–824, Dec. 1999.

[25] D. M. Pozar. *Microwave Engineering*. John Wiley & Sons, New York, third edition, 2005.

[26] J. G. Proakis. *Digital Communications*. McGraw-Hill, third edition, 1995.

[27] J. G. Proakis and D. G. Manolakis. *Digital Signal Processing*. Pearson Education, Inc., fourth edition, 2007.

[28] K. Steinbrich. Influence of semiconducting layers on the attenuation behaviour of single-core power cables. *IEE Proceedings - Generation, Transmission and Distribution*, **152**(2), 271–276, 2005.

[29] G. C. Stone. Partial discharge diagnostics and electrical equipment insulation condition assessment. *IEEE Transactions on Dielectrics and Electrical Insulation*, **12**(5), 891–905, 2005.

[30] C.-T. Tai. Dyadic Green's functions for a coaxial line. *IEEE Trans. Antennas Propagat.*, **31**(2), 355–358, 1983.

[31] H. L. Van Trees. *Detection, Estimation and Modulation Theory, part I*. John Wiley & Sons, Inc., New York, 1968.

[32] J. Veen. *On-line signal analysis of partial discharges in medium-voltage power cables*. Phd thesis, Eindhoven University of Technology, the Netherlands, 2005.